

## REPORT 1222

# A FREE-FLIGHT WIND TUNNEL FOR AERODYNAMIC TESTING AT HYPERSONIC SPEEDS<sup>1</sup>

By ALVIN SEIFF

### SUMMARY

*The supersonic free-flight wind tunnel is a facility at the Ames Laboratory of the NACA in which aerodynamic test models are gun-launched at high speed and directed upstream through the test section of a supersonic wind tunnel. In this way, test Mach numbers up to 10 have been attained and indications are that still higher speeds will be realized. An advantage of this technique is that the air and model temperatures simulate those of flight through the atmosphere. Also the Reynolds numbers are high. Aerodynamic measurements are made from photographic observation of the model flight. Instruments and techniques have been developed for measuring the following aerodynamic properties: drag, initial lift-curve slope, initial pitching-moment-curve slope, center of pressure, skin friction, boundary-layer transition, damping in roll, and aileron effectiveness.*

### INTRODUCTION

A relatively straightforward way to produce hypersonic air flow about an object is to shoot it from a gun at high speed upstream through the test section of a supersonic wind tunnel. The resultant air speed is high, and the speed of sound in the test stream is relatively low. Accordingly, high Mach numbers can be realized with only moderate demands on the performance of the wind tunnel and the gun. For example, if the wind tunnel has a Mach number 2 air stream and the gun fires at 4000 feet per second, the resulting Mach number is approximately 7. For an air-stream Mach number of 3 and a projectile velocity of 8000 feet per second, the test Mach number becomes 15. Thus the air-stream Mach numbers can be kept below values at which there is difficulty with air condensation and still permit the attainment of hypersonic test Mach numbers.

The stagnation-point air temperatures and boundary-layer recovery temperatures which occur in tests of this nature are quite high, made so by the same actions as produce high temperature levels in hypersonic free flight through the atmosphere. For very high Mach numbers at which stagnation temperatures of thousands of degrees Rankine occur in flight, this technique provides a feasible and convenient method of attaining those temperatures. The Reynolds number simulation is also good because the models fly in the relatively dense air of a moderately supersonic air stream.

It can be anticipated, however, that the launching of an aerodynamic model, such as an airplane, from a gun will offer greater problems than would the launching of a simple

projectile, particularly if high speed is the goal. This, then, is one of the problems to be met. Another is the problem of extracting aerodynamic data from the brief flights. It can be foreseen that some aerodynamic properties, such as the drag, will be obtained by procedures that are straightforward, at least in principle. Methods for measuring lift, center of pressure, or boundary-layer skin friction may be less apparent.

Because it offered promise of providing test conditions and data that would be difficult to obtain in other ways, this technique was proposed by H. J. Allen in 1946 as the basis of a facility for hypersonic research at the Ames Laboratory. This proposal resulted in the construction of the supersonic free-flight wind tunnel which was put into operation at the close of 1949. This facility has been used in the ensuing period to study aerodynamic problems in the Mach number range from 4 to 10. The present paper and reference 1 may be considered as progress reports on the development of the facility and technique. The material presented here includes a description of the facility, a discussion of model design and launching, and a discussion of measurement techniques and the accuracies attained.

### NOTATION

$a$	acceleration, ft/sec <sup>2</sup>
$a_1, a_2, a_3$	coefficients of theoretical equation for rolling motion
$a_o$	speed of sound in the test section, ft/sec
$A$	reference area, ft <sup>2</sup>
$C_D$	drag coefficient
$C_{i_r}$	damping-in-roll coefficient
$C_L$	lift coefficient
$C_{L\alpha}$	lift-curve slope, per radian
$C_{m\alpha}$	pitching-moment-curve slope, per radian
$d$	distance decrement, $\frac{1}{2}at^2$ , ft
$D$	drag force, lb
$e_D$	error in drag force, lb
$e_a$	error in acceleration, ft/sec <sup>2</sup>
$e_t$	time error, sec
$e_x$	distance error, ft
$f$	frequency, cps
$I_x$	moment of inertia of model about the longitudinal axis, slug-ft <sup>2</sup>
$I_y$	moment of inertia of model about a transverse axis through the center of gravity, slug-ft <sup>2</sup>

<sup>1</sup>Supersedes recently declassified NACA RM A52A24, "The Ames Supersonic Free-Flight Wind Tunnel," by Alvin Seiff, Carlton S. James, Thomas N. Canning, and Alfred G. Bolisevaln, 1952.

$k$	damping-in-roll constant, equation (30), $\text{sec}^{-1}$
$K$	$\frac{\rho A}{2m}$ , $\text{ft}^{-1}$
$l$	model length, ft
$l_p$	rolling moment due to rolling velocity, lb-ft/radians/sec
$l_a$	rolling moment due to aileron deflection, lb-ft/radian
$L$	lift force, lb
$L_a$	lift-curve slope, lb/radian
$m$	model mass, slugs
$M$	Mach number
$M_a$	Mach number of the wind-tunnel air stream relative to the earth
$M_a$	pitching-moment-curve slope, lb-ft/radian
$p_e$	equilibrium rolling velocity, radians/sec
$p_t$	model rolling velocity as it enters the test section, radians/sec
$q$	dynamic pressure of the air stream relative to the model, $\text{lb/ft}^2$
$s$	compressive stress at model base, $\text{lb/ft}^2$
$t$	time, sec
$T_o$	static temperature of air stream, $^{\circ}\text{R}$
$T_s$	stagnation temperature of air stream relative to model, $^{\circ}\text{R}$
$u_a$	velocity of the air stream relative to the earth, ft/sec
$u_t$	initial velocity in the $x$ direction of the model relative to the air, ft/sec
$u_m$	velocity in the $x$ direction of the model relative to the earth, ft/sec
$u_{m_t}$	initial velocity in the $x$ direction of the model relative to the earth, ft/sec
$u$	velocity in the $x$ direction of the model relative to the air, ft/sec
$v_a$	velocity component of wind-tunnel air stream normal to tunnel axis, ft/sec
$V$	resultant velocity of model relative to the air, ft/sec
$w$	density of material from which model is made, slug/ $\text{ft}^3$
$x_m$	distance parallel to tunnel axis traveled by the model relative to the earth, ft
$x$	distance parallel to tunnel axis traveled by the model relative to the air, ft
$x_{cp}$	location of model center of pressure measured from model nose, ft
$x_{cg}$	location of model center of gravity measured from model nose, ft
$x_G$	gun length, ft
$y$	coordinate normal to tunnel axis, ft
$y_M$	amplitude of swerving motion, ft
$\alpha$	angle of attack, radians
$\alpha_M$	amplitude of pitching oscillation, radians
$\delta$	aileron deflection angle, radians
$\rho$	air density in test section, slugs/ $\text{ft}^3$
$\theta$	relative wind direction measured from $x$ axis, radians

$\phi$	roll position, radians
$\phi_t$	roll position of model as it enters test section, radians

## EQUIPMENT AND TECHNIQUES

## GENERAL ARRANGEMENT

The arrangement of equipment which has been used in the supersonic free-flight tests at the Ames Laboratory is shown in figure 1. A gun for launching the test model is placed in the diffuser of a small supersonic wind tunnel, and provision is made for observing the flight of the model through the test section by means of shadowgraph stations. In most respects the wind tunnel is not unusual. It has interchangeable two-dimensional nozzles for air-stream Mach numbers of 2 and 3, and the test section is 1 foot wide by 2 feet high. The most unusual features are the test section length, which is 18 feet, and the large number of flow observation stations, seven in all. Both these features are fundamental to the use of the wind tunnel for free-flight testing.<sup>2</sup>

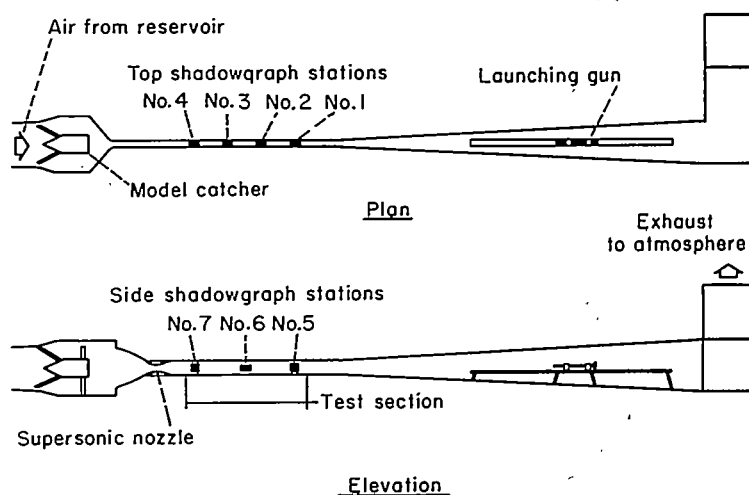


FIGURE 1.—General arrangement of the Ames supersonic free-flight wind tunnel.

Air at elevated pressures up to 6 atmospheres is supplied to the wind tunnel from a large reservoir. Discharge is to the atmosphere through two right-angle bends which act as a light trap. A photograph of the test section and control panel is shown in figure 2.

Photoelectric equipment is used to detect the approach of the model to each shadowgraph station and fire the shadowgraph sparks. The time of firing of the sparks is recorded by a chronograph. The linear and angular positions of the model at each station are recorded in the shadowgraphs. This record of time and position provides the basic data from which aerodynamic forces and moments are computed.

The successful application of this device to aerodynamic testing requires the development of several different aspects of the operation into a workable state. The models must be launched in stable flight without damage and with small dispersion. Electronic equipment must detect the model in its flight, fire the shadowgraph sparks at the correct instants,

<sup>2</sup> The test section is currently being modified to incorporate 18 stations, 9 on the top and 9 on the side, spaced at 3-foot intervals.

produce light bursts of short duration to give crisp model images for position measurement, and time the spark firings with precision. Finally, procedures must be devised for converting this information into aerodynamic data. The remainder of this paper will be concerned with these subjects.

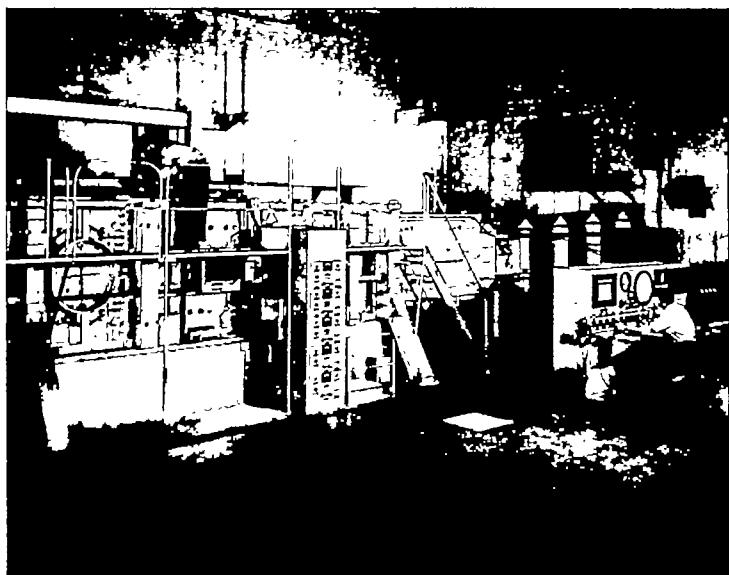


FIGURE 2.—Photograph of test section and control panel.

#### THE DESIGN AND LAUNCHING OF THE TEST MODELS

Launching an aerodynamic model from a gun without destroying it or deforming it, and setting it in flight along a predetermined course is seldom a simple matter and is one that has required considerable development. For designing the model, a fundamental consideration is knowledge of the maximum acceleration that will occur. Furthermore, for attaining high launching speed, the launching acceleration must be held to the minimum possible value. For these reasons, the accelerations which occur in guns are of prime concern to the model designer. A first step toward defining these accelerations is to consider the simplified case of uniform acceleration. The relationship between muzzle velocity and acceleration is then

$$u_m^2 = 2ax_g \quad (1)$$

Thus the projectile acceleration will tend to increase with the square of muzzle velocity. Also, the greater the length over which the acceleration process can be stretched, the lower the acceleration will be, suggesting the desirability of long guns.

The uniform acceleration is the minimum acceleration for a given muzzle velocity in a given length gun, since a lower acceleration at any point along the bore will necessitate a higher acceleration at another point to maintain the specified muzzle velocity. Therefore, peak accelerations will be greater than indicated by equation (1). The values that do occur can be determined reliably only from experiment. The pressure variation in the powder chamber during firing is measured by means of a strain gage. An example of the pressure variations recorded is shown in figure 3. The peak acceleration is calculated from this record by assuming that the peak cham-

ber pressure is applied to the model base.<sup>3</sup> In this way data, such as are shown in figure 4, are collected to define the variation of peak acceleration with muzzle velocity for particular conditions of gun geometry, projectile weight, and powder fineness. Not only does the mean acceleration increase with the square of muzzle velocity according to equation (1) (lower curve, fig. 4), but in addition, the ratio of peak acceleration to mean acceleration increases with increasing muzzle velocity. The resultant rate of rise of peak acceleration with muzzle velocity is very sharp and reaches values in the hundreds of thousands of  $g$ 's.

<sup>3</sup>In general, the pressure at the projectile base is lower than the chamber pressure. The ratio of the two depends mainly on the instantaneous projectile velocity and the distance of the projectile from the powder chamber. At the instant of peak pressure, conditions are such that the two pressures are very nearly equal.

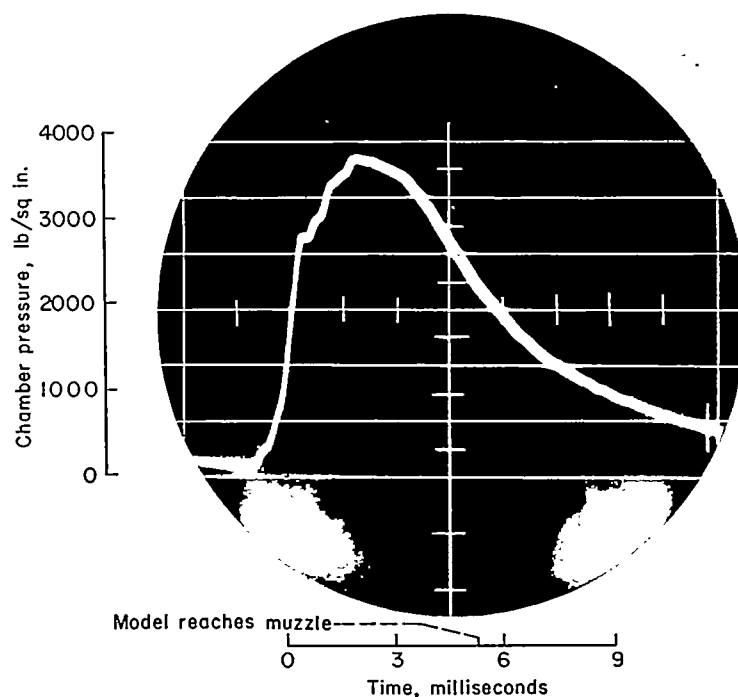


FIGURE 3.—Strain-gage record of chamber pressure in the Ames 1.5-inch smooth-bore gun.

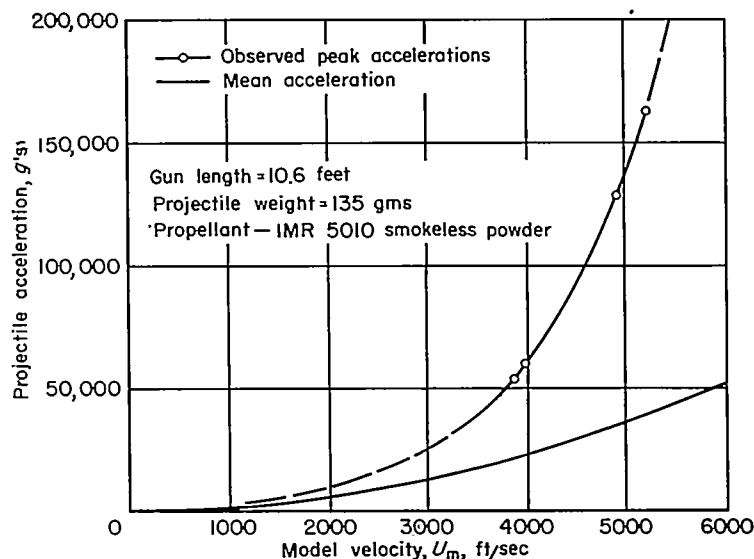


FIGURE 4.—Acceleration data from the Ames 1.5-inch smooth-bore gun.

When the peak launching acceleration for the desired muzzle velocity has been established as described above, the model strength requirements become definite. The stresses due to acceleration must be kept within the bounds of what the materials can withstand. Experience has indicated that the model will deform or fail when the stress exceeds the static yield stress. (An exception to this is the case of a solid cylinder which fills the gun bore and is therefore supported on all sides. When supported in this way, nylon plastic, for example, can be subjected to several times its normal ultimate stress without failure.) A type of failure that frequently defines the acceleration limit is failure due to compressive stress at the model base. The accelerating force transmitted through the base must accelerate the model mass at the specified rate, and Newton's law applied to this situation defines the stress at the base. Consider the case of a solid homogeneous cone of any desired fineness ratio accelerated parallel to its axis. The acceleration for failure at the base depends only on the cone length and its strength-weight ratio.

$$a = 3s/wl \quad (2)$$

For this type of failure and for others, the strength-weight ratio determines the maximum speed with which the model can be fired and is therefore a most important property of the model. For this reason, the aluminum alloy, 75ST, is one of the best commonly available materials for model

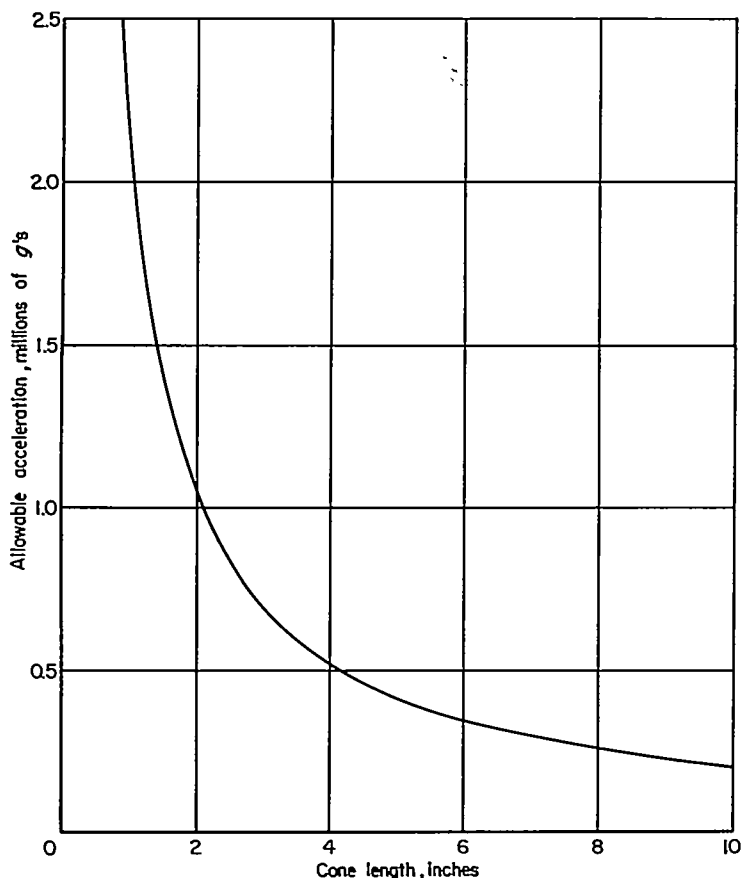


FIGURE 5.—Allowable axial accelerations for solid 75-ST aluminum cones.

fabrication. The maximum allowable accelerations for compressive failure at the base with cones of this material are shown in figure 5 as a function of cone length. This figure shows, for example, that solid cones longer than 4.2 inches will fail at accelerations greater than 500,000 g's. Of course, other types of failure such as column failure with slender bodies and local buckling of thin-walled shells may occur in particular circumstances before compressive failure at the base. Also, the model shape and solidity affect the tolerable acceleration for compressive failure. Therefore, figure 5 should be regarded only as an example of the allowable accelerations for a particular case. It is a favorable example in the sense that the solid homogeneous cone is better able to withstand axial acceleration than are the usual test models.

The effect of increasing the launching velocity, then, is to limit the model scale. The extent of the limitation will depend on particular factors, principally the model shape and the ability of the gun to produce high speed with low acceleration.

Several considerations other than strength enter into the model design. Aerodynamic stability is one. As with full-scale aircraft, the center of gravity must be located to give stability, by ballasting the nose or hollowing the base. In a few cases, spin stability has been used, but normally it has been avoided because it may alter aerodynamic properties. Another consideration is that the weight and moment of inertia of the model must be adjusted to give a sufficient response to the aerodynamic forces and moments. The requirements in this respect will be discussed in later sections. An important consideration is the protection and alinement of the model during firing. This is accomplished by use of a sabot which is an auxiliary part of the projectile, integral with the model within the gun, but separate after emerging from the barrel. The sabot separates the model from the powder gases, holds it free of the gun wall, and applies the accelerating force to the model. In flight, it must separate cleanly with a minimum of disturbance. The number of possible sabots is nearly as varied as the number of possible models. As examples of the variety to be encountered, a few specific ones will be described. A typical sabot for fin-stabilized bodies of revolution such as the one on the left in figure 6 (a) is shown at the corresponding position in figure 6 (b). To hold the body alined in the gun, it makes use of fingers set in the quadrants between the fins. In flight, the fingers separate radially due to air force on their beveled leading edges. Sabots of this general type apparently were first used at the Naval Ordnance Laboratory, White Oaks, Maryland. A sabot which has been used for launching cones and similar models is shown at the center of the figure. The model shown is an aerodynamically stable cone, made stable by thin-walled construction over the after 70 percent of its length. The cone base is seated on a cylindrical sabot and is ground to fit and sealed with stopcock grease. The hollow volume between the parts is then evacuated through a fine hole in the sabot base. This provides a firm holding action which will hold the model on the sabot for lateral accelerations up to 10 g's. The evacuation hole is

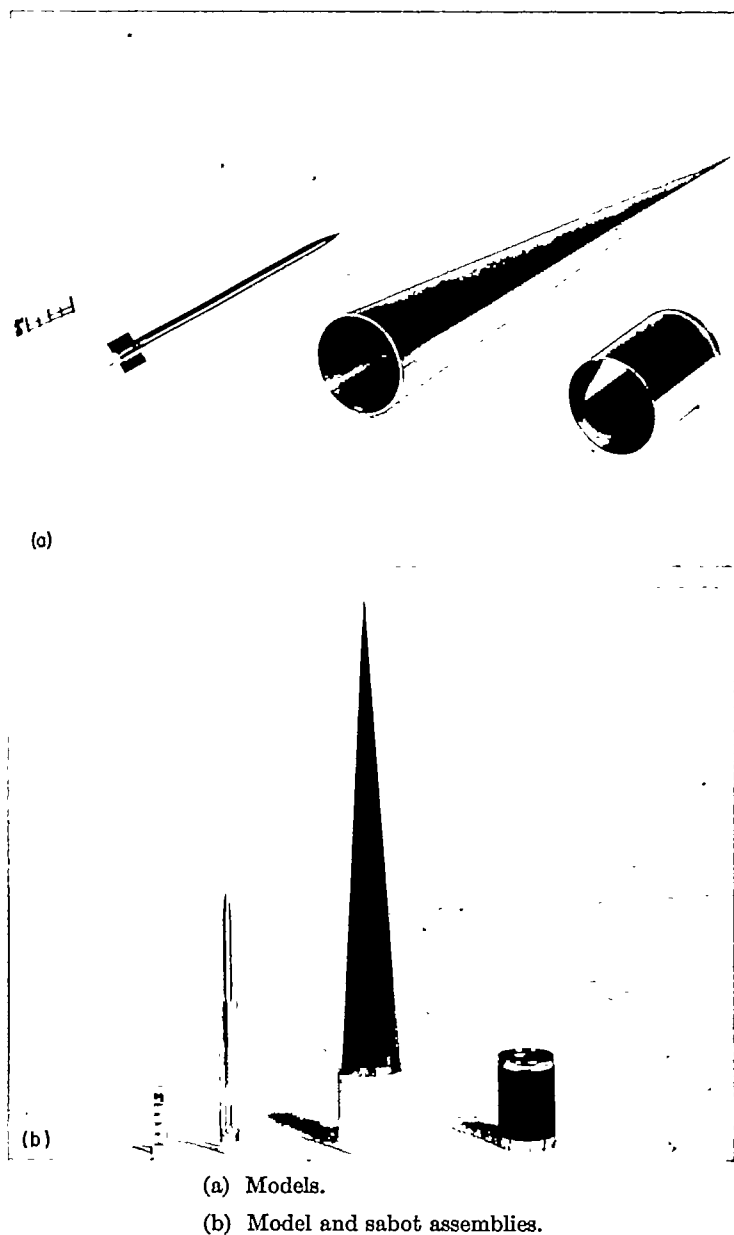


FIGURE 6.—Representative models and sabots.

sealed with a piece of plastic tape. On firing, the tape is ruptured by the pressure and powder gases accumulated inside the model. At the gun muzzle, the gas pressure provides positive separating action. At the right in figure 6, there is shown a model devised for the measurement of skin friction. It is a thin-walled tube (wall thickness less than  $\frac{1}{2}$  inch) with a beveled leading edge. These models were spin stabilized by firing from a rifled gun. For protection from the rifling, the models were made undersize and wrapped in plastic film before loading. The acceleration load was transmitted to the model through a rifled aluminum disk which also imparted spin through friction at the model base.

#### RANGE OF TEST CONDITIONS

The Mach number range of the supersonic free-flight wind tunnel is shown in figure 7 for model launching speeds

from 1000 to 7000 feet per second. The Mach number is calculated from the resultant speed of the air relative to the model compared to the speed of sound in the test section.

$$M = \frac{u_m + u_a}{a_o} = \frac{u_m}{a_o} + M_a \quad (3)$$

The speed of sound,  $a_o$ , for the existing conditions of an air reservoir at room temperature and an air-stream Mach number of 2, is about 830 feet per second.

By utilizing the tunnel with still air and with air flow at  $M=2$ , the entire supersonic speed range up to a Mach number of 10 is covered. The selected upper limit of test Mach number is arbitrary. Missile models about 3 inches long have been launched at speeds up to 7000 feet per second. One is shown in flight at a Mach number of 10 in figure 8. Indications are that small-scale models can be launched somewhat faster and that, by use of a Mach number 3 nozzle, Mach numbers up to 15 will be attained.

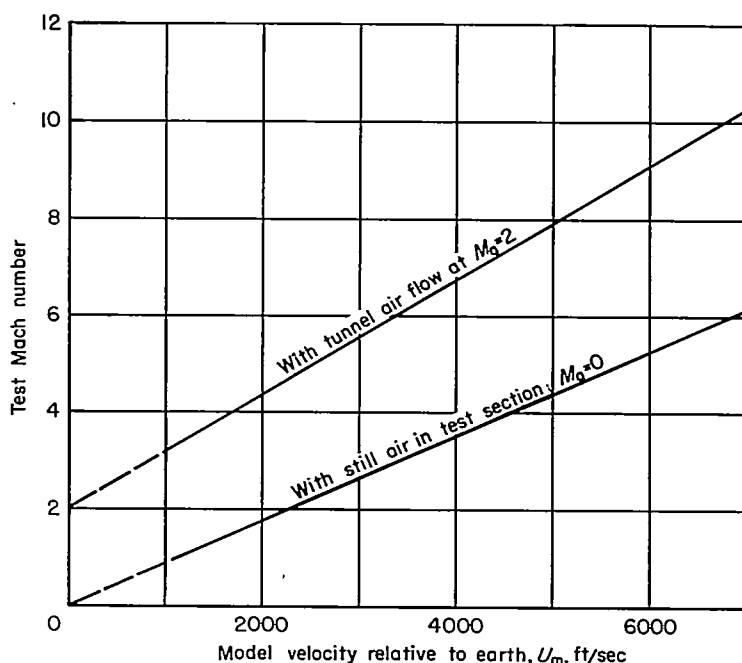
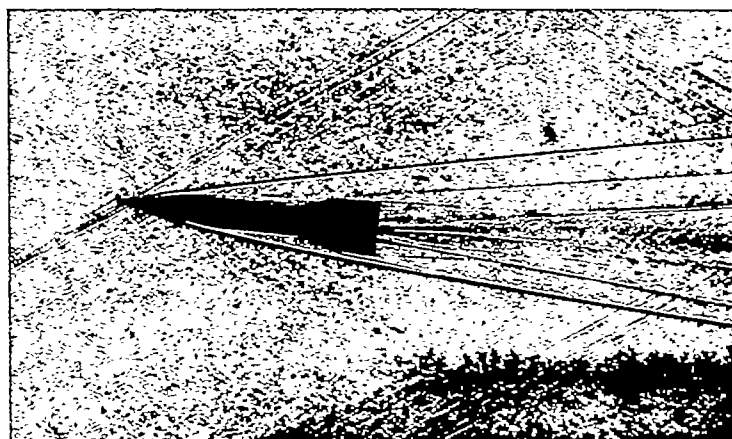


FIGURE 7.—Current Mach number range.

FIGURE 8.—Model in flight at  $M=10$ ,  $R=16$  million,  $\alpha=6^\circ$ .

The Reynolds number limits are shown in figures 9 and 10. The Reynolds number per inch (fig. 9) increases with increasing Mach number because the free-stream air density and viscosity remain fixed as the Mach number is increased. The maximum length Reynolds numbers attainable (fig. 10) have been calculated by use of the model length limitations implicit in figures 4 and 5. Below a Mach number of 8, the model was arbitrarily assumed limited in length to 12 inches. No limit due to launching acceleration exists in this area. Above  $M=8$ , the length is forced down by the acceleration characteristics of the gun and model. Quite high maximum Reynolds numbers, above 40 million over most of the speed range are indicated. To a degree this figure is deceptive. It applies only to solid cones, and has been derived without regard for proper model mass characteristics, stability, etc. Therefore, for the usual case, a somewhat lower maximum curve than the one shown would apply, but would still be measurable in the tens of millions.

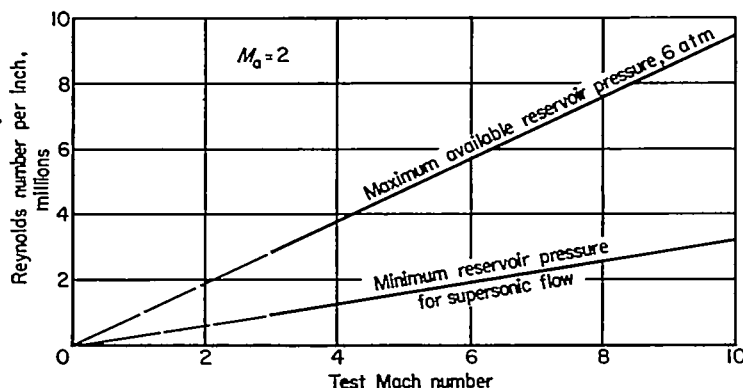


FIGURE 9.—Variation with test Mach number of the Reynolds number per inch.

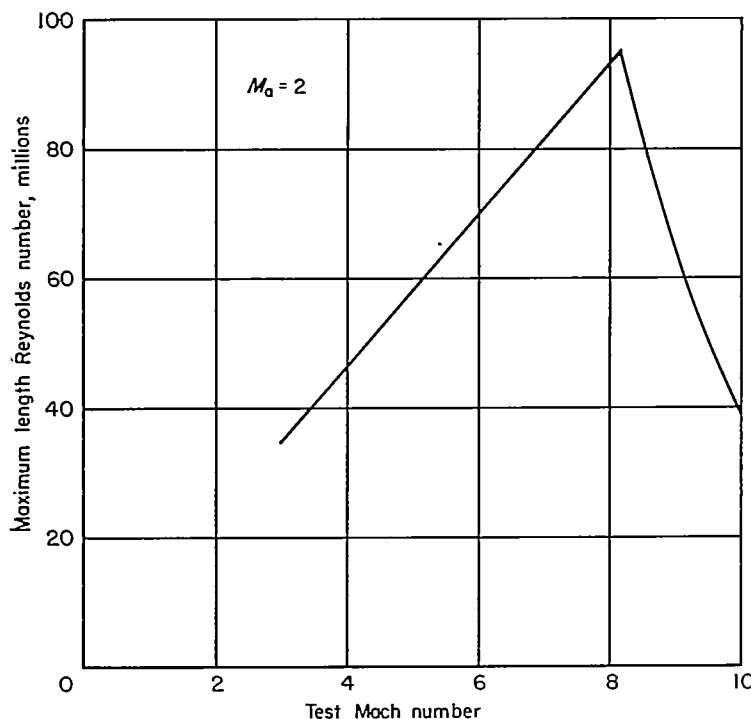


FIGURE 10.—Maximum length Reynolds numbers.

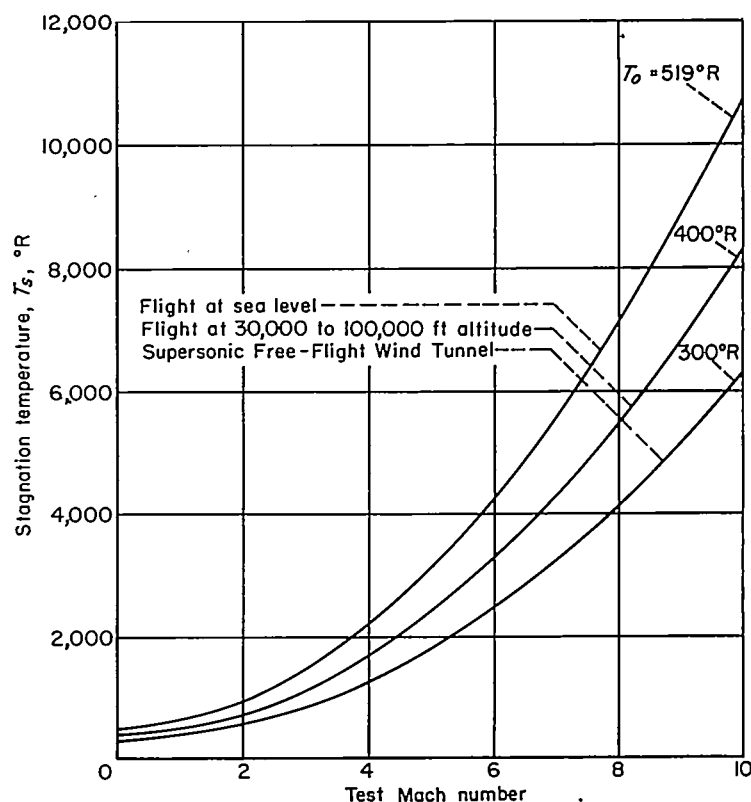


FIGURE 11.—Comparison of test stagnation temperatures with flight stagnation temperatures.

The static air temperature in the test section for the unheated air supply expanded to a Mach number of 2 is approximately 300° Rankine. This is about three-fourths the temperature in the isothermal layer of the atmosphere—at altitudes from 30,000 to 100,000 feet. Accordingly, the test stagnation temperatures are about three-fourths the flight stagnation temperatures in this altitude range as is shown in figure 11. By comparison the body surface temperatures remain relatively cold, not much higher than room temperature. This is due to the short duration of the test flights—about 10 to 20 milliseconds. Normally the body surface temperature rise due to aerodynamic heating in flight is of the order of 20° to 50° Fahrenheit except in the region of a pointed tip or a sharp leading edge. At these locations, calculations have indicated a temperature rise of a few hundred degrees in a limited region (hundredths of an inch long) near the tip. For the most part, however, it is a good approximation to assume negligible temperature rise in flight, so for room-temperature models, the ratio of wall temperature to stream temperature is near 1.8. For flight in the isothermal altitude range, this corresponds to a body surface temperature of 260° Fahrenheit.

#### EQUIPMENT FOR RECORDING THE MODEL FLIGHT PATH

The method used for measurement of aerodynamic characteristics in the subject facility is basically the same as is used in ballistics ranges. The present facility, however, is limited in length, being confined to the test section of a supersonic

wind tunnel,<sup>4</sup> and this makes it necessary to measure time and position with unusual accuracy. As will be shown subsequently, for some measurements, errors must be held to a few thousandths of an inch in position and a few hundredths of a microsecond in time. The way in which these requirements are met will be described in this section. The first part will deal with the shadowgraph recording of model position, and the latter part with the precise measurement of the times at which the shadowgraph sparks fire.

For the shadowgraph stations from which the basic measurements are obtained—those which view the horizontal plane—a parallel light system was selected so that the models and their positions would be projected at true scale and without distortion. The optical system of these stations is indicated schematically in figure 12. As indicated therein, the light sources are high intensity sparks. Light produced by the sparks is made parallel by reflection from spherical mirrors and is directed through optical glass windows across the test section where it falls on 8- by 10-inch photographic plates located just above the upper windows. A scale used to measure linear and angular positions of the models is located just below the film plates and is recorded along the edge of each shadowgraph as shown in figure 13. The firing of the sparks, which is initiated by the interruption of the photobeams at each station, is electronically delayed to let the model reach the desired position in the field of view of the station.

Characteristics of the system that are important in providing reliable position data are: a spark of short duration and small aperture to give a sharp shadow image; a light system aligned and calibrated to project the model position from the plane of flight to the plane of the photograph

<sup>4</sup> The length of the test section is limited by the growth of boundary layer on the wind tunnel walls. With too long a test section, the boundary layer would fill the channel. With the dimensions used here, the boundary layer on each side wall fills one-fourth the width of the channel at the downstream end.

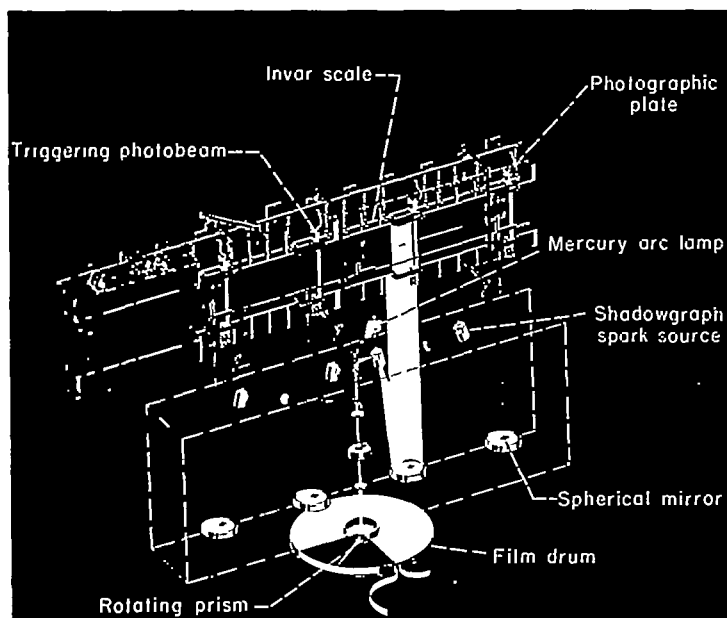


FIGURE 12.—Schematic diagram of shadowgraph and chronograph systems.

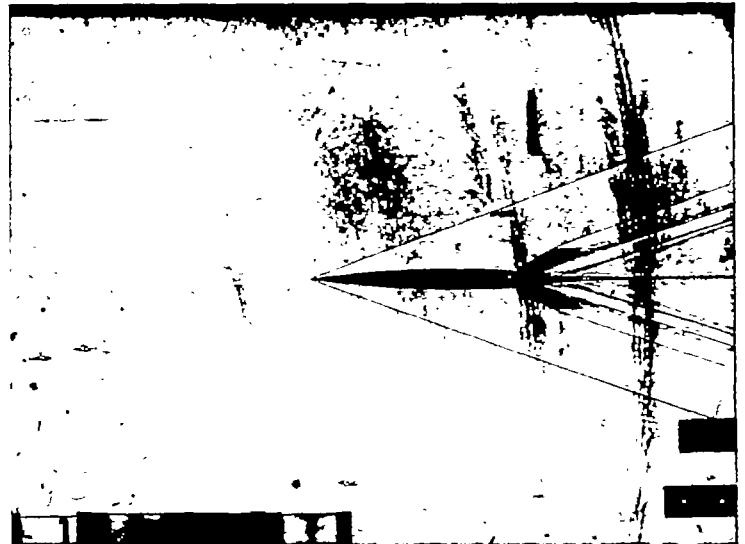


FIGURE 13.—Shadowgraph picture showing the full field of view and the measuring scale.

without causing error; and, a model detection system to fire the sparks reliably so that it can be expected that when a model is launched, data will be recorded.

The photoelectric system for firing the sparks.—Two inches ahead of each shadowgraph station, light from an incandescent lamp is collimated by a strip segment of a three-dimensional lens to form a parallel beam 8 inches wide by  $\frac{1}{4}$  inch thick which is directed across the height of the wind tunnel to form the photobeam.<sup>5</sup> Below the wind tunnel, the light is collected by a similar lens segment and focused on a phototube to produce a photoelectric current of about 6 microamps. Small changes in this current occur momentarily when a model interrupts the photobeam. The current pulse produced is of high frequency and represents very little electrical charge so that care must be taken to avoid losing it to ground through the random capacity of the system. The model signal is taken off a resistor as a voltage pulse and is amplified eight-thousand fold in three stages to control the operation of a thyatron which passes the trigger impulse to fire the spark.<sup>6</sup>

Two kinds of trouble were encountered in the development of the above system that are worth noting. Because it was required to be very sensitive, spurious signals could be introduced by vibrating the optical parts and electronic components in the first stages of amplification. The result at first was that the wind-tunnel noise and vibration were sufficient to fire the sparks as fast as the condensers recharged. After some development, this was corrected by shock-mounting sensitive parts and filtering out low frequencies which contributed to the noise but not to the signal generated by the passage of the model. A second problem was a tendency of the various stations to interfere. For example, station 1, when fired, would also set off station 2. This was found to be due primarily to electromagnetic

<sup>5</sup> Because the photoelectric light beam is very near the shadowgraph station, it tends to fog-expose the shadowgraph film. This is prevented by use of red photobeams and red insensitive shadowgraph plates.

<sup>6</sup> See reference 2 for information on the electronic circuits mentioned here and elsewhere in this report.

radiation from the high-voltage spark-trigger leads and was corrected by shortening and shielding the leads. The development and improvement of this equipment was carried on chiefly by J. R. Jedlicka and W. J. Kerwin in 1951-52. At the present time, its reliability is good. Better than 19 out of 20 pictures attempted are recorded. The failures that occur can be traced to defective circuit elements or equally definite causes.

**The Shadowgraph sparks.**—The demands that are imposed on the light source in this application are really very severe. The duration must be a small fraction of a microsecond to effectively "stop" the projectile motion on the film. The intensity must be sufficient to expose film in this length of time at a distance of 7 feet from the source, the focal length of the collimating mirrors. Fortunately, considerable development of such a light source had been completed before the present facility was built, at the Ballistics Research Laboratory, Aberdeen, Maryland (ref. 3). The BRL spark design was used in the present facility. It consists of two aluminum electrodes set at a gap of about 0.1 inch connected by short leads to the opposite plates of a condenser (in this case, 0.1 microfarad) charged to 6000 volts. The spark is fired by ionizing the air in the gap, using the high voltage output of an induction coil applied to a third electrode, the trigger electrode. The total light output depends primarily on the energy stored; that is, on the voltage and capacity. The duration depends on the natural frequency and damping of the oscillatory discharge which occurs in this capacitive-inductive loop. Experimentally, the effective duration of the spark is found, from examination of the blur produced at the base of fast moving projectiles, to be about  $\frac{1}{2}$  microsecond. The total duration (time during which any measurable current is flowing in the loop) is greater.

Sparks of shorter duration have been developed using an arrangement suggested by L. S. G. Kovasznay, reference 4, consisting of multiple condensers surrounding the electrodes to reduce the inductance of the circuit and thereby increase its natural frequency. At Ames Laboratory, W. J. Kerwin has applied this idea to obtain sparks with a natural frequency of 4 megacycles. In addition he has controlled the resistance in the loop to damp the oscillation in the first half cycle. The resulting sparks have a duration of 0.1 microsecond as shown by an oscilloscope record of the current in the discharge. There results an improvement in sharpness and flow detail in the shadowgraph picture.

**Light alinement and calibration.**—The essential characteristic of the shadowgraph optical system is that it must project the model image from the plane of flight to the photographic plate without introducing error. In principle, this can be accomplished either by alinement or by calibration, but in practice a perfectly alined system is impossible to produce. Since it was proposed to measure positions accurate to 0.001 inch, the allowable error in light ray direction became  $7 \times 10^{-5}$  radians or 0.004°. There are several reasons why the system cannot be alined and maintained to this degree of perfection: The collimating mirrors and test-section windows are not optically perfect; the light source is mounted off-axis of the collimating mirrors; and the mounting

frames are not perfectly rigid and are subject to temperature effects.

Nevertheless, the optical system was alined with some care in order to reduce corrections to a minimum. The relative positions of spark and collimating mirror were carefully adjusted to make the individual beams very nearly parallel within themselves. Also, the light beams were made vertical by rotating the mirrors. Then the system was calibrated. To determine the residual errors in parallelism within each beam, a grid plate was placed in each shadowgraph station and photographed. The plate covered the entire 8- by 10-inch field of view and was perforated with 63 sharp-edged holes placed at the corners of 1-inch squares. The spacing of the hole images was compared with the physical spacing of the holes in the plate to determine the errors in parallelism. Errors were found which were large enough to cause model position errors of a few thousandths of an inch in the worst places. Then a 5-foot-long Invar bar whose precise length had been measured in a gage laboratory was set up in the test section with one end in a given shadowgraph station and the other end in an adjacent station and the two ends were photographed. Thus, the image positions in the two stations corresponding to a precisely known distance interval in the test section were recorded. This operation was repeated for each pair of stations at three levels within the test section to define the interval relationships of the four stations. The 17-foot Invar scale which extends the full length of the test section and appears in the shadowgraph pictures (fig. 13) was thus calibrated.

To prevent loss of the calibration due to shifting of the mirrors and the sparks, there was devised a photographic reference system to detect the changes and provide a basis for correction. This system records the images of sharp-edged holes in thin plates placed at two elevations in each shadowgraph light beam. When the light beam tilts, the spacing of the hole images changes and the amount of change is a direct measure of the angular disturbance as illustrated in figure 14. The reference holes are separated vertically by 3 feet. This is 2.4 times the average distance of projection of the model image. There is, therefore, an effective magnification of 2.4; that is, a change in light direction causing 0.0020-inch change in the model position will appear as a 0.0048-inch change in the reference hole spacing. This makes the resolution of the system good and has still more fundamental significance, namely, that the reference hole itself can be physically displaced by 0.005 inch before causing a 0.002-inch error in position. In contrast, a mirror edge need tilt by only 0.0008 inch to cause the same error. Appreciable corrections from the reference system are routinely applied. That the corrections are successful in removing errors is indicated by checks that have been made from time to time of the over-all accuracy of length measurement by rephotographing the 5-foot length standard placed at random locations in the test section. The length of the bar has always been measured correct to within 0.003 inch and usually closer than that.

In the reading of model positions from the shadowgraph plates, additional error is caused by the lack of sharpness of the model edges in the pictures. When examined under a

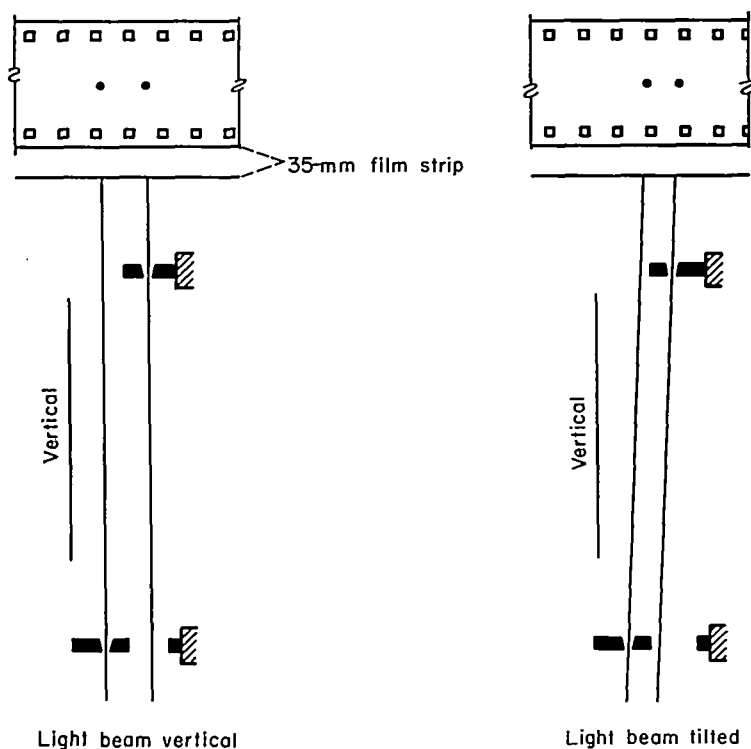


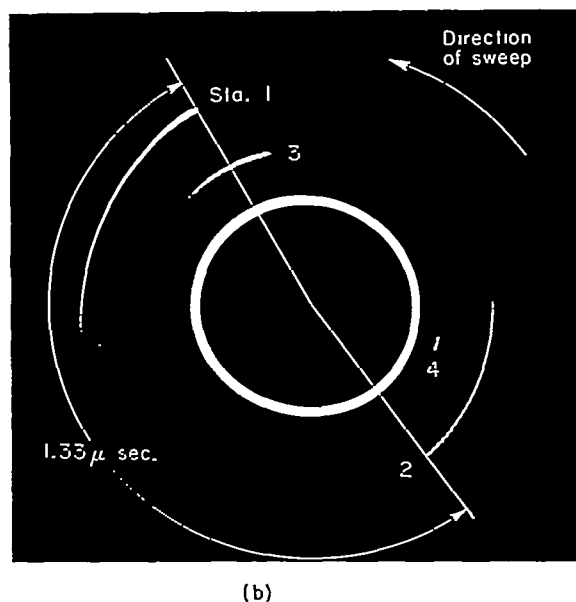
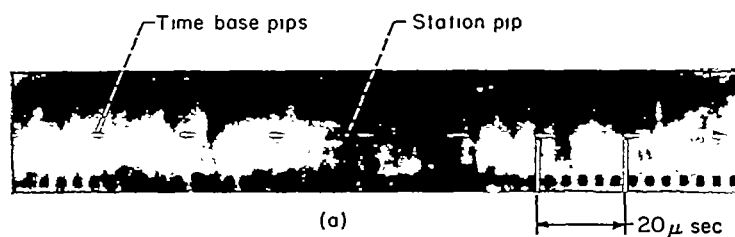
FIGURE 14.—System used to detect light beam tilt.

microscope, these edges are blurred, several thousandths of an inch wide due to the finite aperture size of the source and to the finite duration of the spark. The requirement, however, is not to read absolute positions, but to read intervals, for example, the distance covered between the firings of sparks 1 and 2. If corresponding points in the images from two adjacent stations are used, the interval can be read more precisely than the absolute positions. In making such readings with a microscope (using a coordinate comparator of the type used by astronomers to measure star coordinates), different observers will read the distance intervals with a disagreement depending on the quality of the images, but usually less than 0.003 inch. Even when the errors due to light alignment and the errors due to reading are considered, the interval readings are thought to be accurate to within 0.003 inch on the average.

**Chronographs.**—Two chronographs have been developed for this facility. One was put into operation when the facility was built and the other was added later. In the original chronograph, electronic transmission of the time signals to the point of recording was avoided because it was feared that the signals might have different transmission times and cause error. Therefore the signals were transmitted optically to the recording film. The transmission times were then known to differ by less than 0.01 microsecond. With this instrument as a standard, a second, all-electronic, chronograph was developed. The latter one has greater time resolution and has been shown to give results compatible with those of the optical chronograph.

The principle of the optical chronograph is shown schematically in figure 12. When a spark fires, part of the light is directed by a system of lenses and mirrors to a film drum where it produces a spot exposure on a 35-mm film strip. At the center of the drum there is a 45° mirror rotating at high speed to distribute the time signals from the four

sparks along the 15-foot circumference of the drum. If the speed of rotation of the mirror were precisely known and constant during a revolution, and if the film shrinkage over the 15-foot length were assured uniform, the above data would be sufficient to define the time intervals. Since in practice these conditions are not accurately fulfilled, a second series of closely spaced marks is recorded on the film to serve as a time standard. This set of pips results from the flashing of a H-6 lamp, a high-pressure mercury vapor lamp, under the control of a piezoelectric crystal. Usually, the lamp is flashed at 20-microsecond intervals although other intervals can be selected as required. A small segment of the 35-mm film record showing some time-base pips and one station pip is reproduced in figure 15 (a). The most important requirement of the time-base intervals is that they be equal since relative accuracy rather than absolute accuracy is the crucial requirement. Actually both relative and absolute accuracy are attained, the former as is evidenced by the uniformity of spacing of the H-6 pips (uniform within 0.5 percent or 0.1 microsecond), and the latter by checking against the Bureau of Standards frequency calibration signal. The reading of time intervals between spark firings proceeds by counting the 20-microsecond time-base intervals and interpolating the station pip positions in the intervals where they occur. With good records, the readings of different observers will agree within 0.1 microsecond and since there are no known systematic errors of this magnitude, the instrument is believed to be this accurate.



(a) Optical chronograph.

(b) Electronic chronograph.

FIGURE 15.—Film records from the two chronographs.

The second chronograph uses commercially available electronic-counter chronographs, which resolve time to the nearest  $\frac{1}{2}$  microsecond, together with an interpolating circuit to determine the fractional parts of a microsecond in each interstation interval. The interpolating circuit was invented and developed at the Ames Laboratory by R. O. Briggs and W. J. Kerwin. It consists of an oscilloscope tracing a circular pattern with a frequency of 400 kc or one turn every 2.5 microseconds. When a spark station fires, an electrical pulse is sent to the interpolator and the pattern is momentarily brightened. A radius-change circuit then acts to decrease the radius of the circular trace for the record of the next station, and the process repeats for the four-station group producing a pattern of four circles each visible only during the time the spark is on (fig. 15 (b)). Any one time interval may be thought of as some whole number of 2.5 microsecond intervals plus a fractional interval. The whole number of turns is deduced from the readings of the counter chronographs. The fractional part is read from the oscilloscope record.

The resolution of this device is very good—the time records can easily be read to the nearest 0.01 microsecond. The accuracy, however, depends on getting the signal from the spark to the interpolator in exactly equal times and also depends on having equal duration characteristics in the four sparks. The latter point is really very fundamental to the whole proposition of accurate time and distance measurement, and has been studied by comparing the current-time curves of the four sparks with an oscilloscope and working with the circuits until the four sparks had similar curves. Also, the obvious precaution of using the same circuit components and lead lengths in each station has been observed. As a result, it is believed that the accuracy of this instrument is not far different from its resolution, namely, near 0.01 microsecond. Comparisons have been made of time measurements with the two independent chronographs and the intervals are found to agree within the normal resolution of the optical chronograph, 0.1 microsecond, when the latter is free of pip overlaps. Frequently, the disagreement is of the order of hundredths of a microsecond.

#### MEASUREMENT OF AERODYNAMIC QUANTITIES

As in ballistics ranges, aerodynamic forces and moments are deduced in this facility from their effect on the model flight path. Drag causes the model to decelerate. Lift causes the model to depart from straight-line flight. Pitching moment causes angular acceleration about a transverse axis. Similarly, other aerodynamic quantities will affect the model flight. The effect is recorded and the cause is deduced. In addition, considerable information is obtained directly from the shadowgraph pictures concerning the state of the boundary layer, laminar or turbulent; the location of transition; the existence of separated flow where it occurs; etc. The various measurement procedures will now be described. The first one, the measurement of drag, will be given rather completely as typical of the procedures used. For brevity, the other procedures will be described in principle and not in detail.

#### DRAG MEASUREMENT

The record from which the drag is derived is the time-distance history from the four shadowgraph stations which photograph the horizontal plane (giving three distance intervals) and the corresponding time intervals. The average velocity in the successive intervals decreases progressively and the rate of decrease is a measure of the drag.

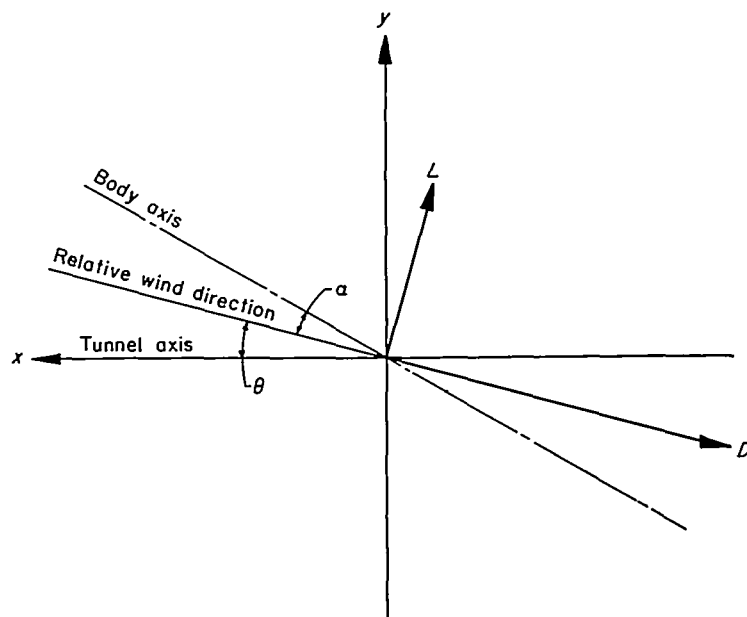


FIGURE 16.—Vector diagram of lift and drag.

The equation for computing the drag coefficient is developed by writing Newton's second law for the force and acceleration components parallel to the tunnel axis. Since the model flight paths are not, in general, perfectly parallel to the tunnel axis, and since the models oscillate in pitch as they fly, there exists a variable component of lift force acting parallel to the tunnel axis as can be seen from figure 16, and the acceleration equation becomes

$$D \cos \theta + L \sin \theta = -m \frac{du}{dt} \quad (4)$$

Since  $\theta$  never exceeds  $2^\circ$ , equation (4) may be written

$$(C_D + C_L \theta) q A = -m \frac{du}{dt} \quad (5)$$

Assuming a linear lift curve,

$$C_L \theta = C_{L\alpha} \alpha \quad (6)$$

The component of lift force along the  $x$  axis is therefore a product of the small quantities,  $\alpha$  and  $\theta$ , and will normally be negligible compared to  $C_D$ . In cases where this term can be omitted, equation (5) reduces to

$$C_D q A = -m \frac{du}{dt} \quad (7)$$

The approximate expression for dynamic pressure,  $\frac{1}{2} \rho u^2$ , differs by less than 0.1 percent from the exact expression,  $\frac{1}{2} \rho V^2$ , because the lateral components of velocity are small.

This approximate expression is inserted in equation (7) to obtain

$$C_D \frac{1}{2} \rho u^2 A = -m \frac{du}{dt} \quad (8)$$

or

$$KC_D dt = -\frac{du}{u^2} \quad \text{where } K = \frac{\rho A}{2m} \quad (9)$$

Using the lower limits,  $x=0$  and  $u=u_i$  when  $t=0$ , we integrate equation (9) twice to get the following logarithmic expression:

$$KC_D x = 1n(KC_D u_i t + 1) \quad (10)$$

Equation (10) cannot be solved for  $C_D$  explicitly. To facilitate use of the equation, the logarithm is expanded in the infinite series,

$$KC_D x = KC_D u_i t - \frac{1}{2} (KC_D u_i t)^2 + \frac{1}{3} (KC_D u_i t)^3 - \dots - \frac{(-1)^{n-1}}{n} (KC_D u_i t)^n \quad (11)$$

Noting that

$$x = x_m + u_a t$$

and

$$u_i = u_{m_i} + u_a$$

and dividing through by  $KC_D$  yields

$$x_m = u_{m_i} t - \frac{1}{2} (KC_D) (u_i t)^2 + \frac{1}{3} (KC_D)^2 (u_i t)^3 - \dots + \frac{1}{n} (-KC_D)^{n-1} (u_i t)^n \quad (12)$$

This is the required relationship between the time-distance data and the drag coefficient. The terms

$$x_m = u_{m_i} t - \frac{1}{2} (KC_D u_i^2) t^2$$

are the equation of uniformly decelerated motion. ( $KC_D u_i^2$  is the deceleration at  $t=0$ ). The additional terms are required to account for the decrease in dynamic pressure with time as the model decelerates. The series converges rapidly. Terms in powers of  $t$  greater than 4 are rarely significant.

The quantities  $x_m$ ,  $t$ , and  $K$  in equation (12) are obtained from the time-distance record, from model measurements, and from the air-stream calibration. Because there are two unknowns,  $u_{m_i}$  and  $C_D$ , two numerically independent equations must be written from equation (12) using time and distance data from three stations. The two equations are solved simultaneously for  $C_D$  by an iterative procedure which first neglects the higher order terms and then corrects for them. The data from the four shadowgraph stations can be combined three at a time in four ways to produce four values of drag coefficient. The average of the four is assumed to be the best experimental value. A least squares procedure would indicate the most probable drag value but would complicate the data reduction without significantly improving the results since the scatter of the four results is typically 2 percent.

It has been assumed above that  $C_D$  is constant through the test section whereas for the usual case of a model oscil-

lating in pitch, it is not. The variations in  $C_D$  that occur are usually relatively small but may become large for large pitching amplitudes at high frequency if the lift-curve slope is large. Good testing procedure requires that the drag coefficient be held nearly constant (say within 5 percent) by regulation of the above variables. If this is done, then it can be assumed that the mean drag coefficient measured is representative of the root-mean-square angle of attack and an approximate correction is applied on this basis for the drag due to lift.

Accuracy required in the time-distance measurements.—The  $x$  component of motion of test models in the supersonic free-flight wind tunnel can for the most part be closely approximated by the equation for uniformly decelerated motion,

$$x = u_i t - \frac{1}{2} a t^2 \quad (13)$$

The main features of the accuracy problem can be studied from this equation with a considerable gain in clarity and simplicity over the use of equation (12). The drag enters equation (13) as it affects the deceleration.

$$a = D/m \quad (14)$$

The deceleration is thus proportional to the drag as is the term,  $\frac{1}{2} a t^2$ , hereinafter called the distance decrement and given the symbol,  $d$ . The distance decrement is, as its name implies, a physical distance. It is the difference,  $u_i t - x$ , between the distance traveled in time  $t$  without deceleration and the distance traveled in time  $t$  with the given deceleration. Its physical significance is illustrated graphically in figure 17.

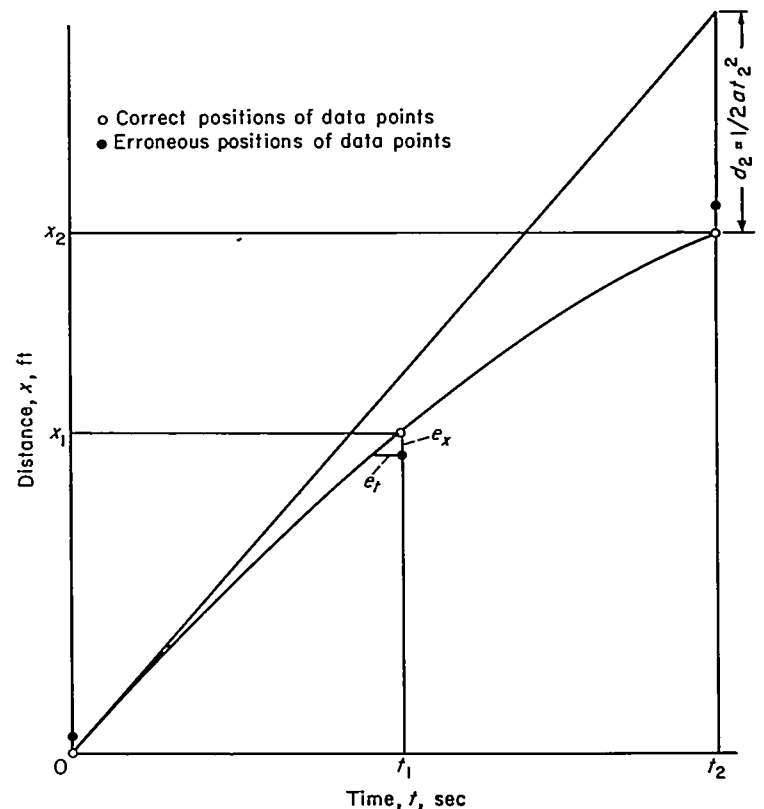


FIGURE 17.—Illustration of the accuracy problem for drag measurement.

Consider the problem of error in  $x$  with  $t$  exactly accurate. Consider also that the initial velocity,  $u$ , at  $t=0$  is exactly known. Then at time,  $t_2$ , in figure 17, the measurement of drag will be simply a measurement of the distance decrement, and the percentage error in the measured distance decrement will also be the percentage error in drag.

$$e_x/d = e_D/D \quad (15)$$

For example, if the distance decrement is 0.1 inch, an error in  $x$  of 0.01 inch will cause a 10-percent error in drag.

Actually, however, the initial velocity of the model is unknown and must be deduced from the time-distance measurements. To do so requires the use of data from three stations which define two intervals. The notation is explained in figure 17.

$$\left. \begin{aligned} x_1 &= u t_1 - \frac{1}{2} a t_1^2 \\ x_2 &= u t_2 - \frac{1}{2} a t_2^2 \end{aligned} \right\} \quad (16)$$

Combining these equations to eliminate the initial velocity and solving for the deceleration yields the following equation:

$$a = \frac{2}{t_2 - t_1} \left( \frac{x_1}{t_1} - \frac{x_2}{t_2} \right) \quad (17)$$

Errors in  $x$  will now be introduced into equation (17). The worst deceleration measurement will occur when the maximum error,  $e_x$ , occurs at all three stations, distributed as shown in figure 17. With these distance errors present, the deceleration is wrong in the amount  $e_a$ .

$$a + e_a = \frac{2}{t_2 - t_1} \left( \frac{x_1 - 2e_x}{t_1} - \frac{x_2}{t_2} \right) \quad (18)$$

$$e_a = -4e_x \frac{t_2/t_1}{t_2^2(1 - t_1/t_2)} \quad (19)$$

$$e_a/a = e_D/D = -2 \frac{e_x}{d_2} \frac{t_2/t_1}{1 - t_1/t_2} \quad (20)$$

Equation (20) shows the worst error in drag for a given maximum error in  $x$  and a given distance decrement, and differs from equation (15) by the factor  $(2t_2/t_1)/[1 - (t_1/t_2)]$  which, for equal spacing of the stations, has the value 8. Therefore, in the absence of the precise knowledge of  $u$ , which was assumed in writing equation (15), the error in drag is increased by a factor of 8 for the worst case of cumulative error.

Equation (20) indicates a procedure having the following steps for estimating the distance accuracy requirements:

(1) From data on the model mass and air-stream dynamic pressure, etc., and using an estimate of the drag coefficient, calculate the distance decrement.

(2) Specify the acceptable percentage inaccuracy in drag and take that percent of the distance decrement. This is the accuracy required with  $u$  known.

(3) Divide the distance error of step (2) by the factor indicated in equation (20).

Example:

$$\begin{aligned} d_2 &= 1.0 \text{ inch} \\ \text{desired accuracy in } C_D &\text{ of 2 percent} \\ 0.02 d_2 &= 0.020 \text{ inch} \\ e_x &= 0.020/8 = 0.0025 \text{ inch} \end{aligned}$$

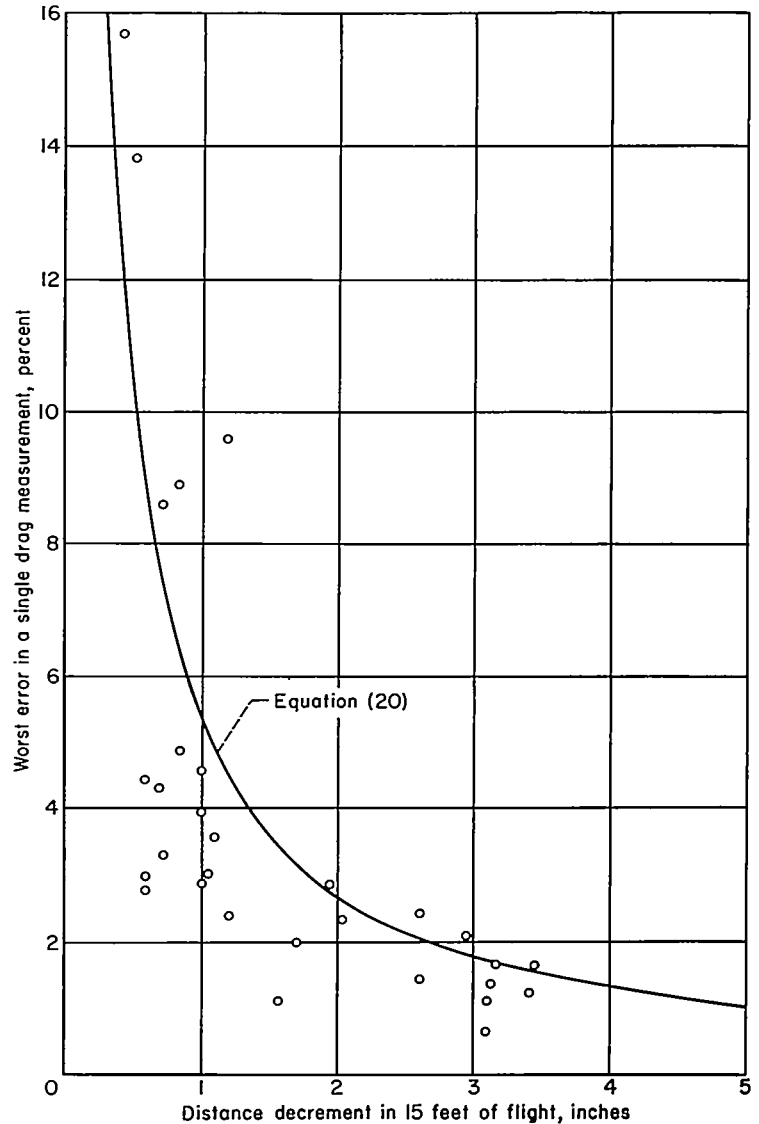


FIGURE 18.—Drag accuracy as a function of distance decrement.

This is the tolerable error in  $x$  for a single measurement with the worst combination of errors. For repeated measurements with random errors, a somewhat larger error in  $x$  can be allowed and will be averaged out.

Equation (20) has been applied to estimating the largest error in an individual measurement of drag coefficient that will occur in the supersonic free-flight wind tunnel with distance errors of 0.003 inch and time accurate. This estimate has been plotted against distance decrement in figure 18. Plotted on this figure for comparison are data on the scatter of drag measurements taken from experimental results in the facility with a variety of test models. The scatter of the four drag measurements obtained with a single round is a result of errors in measuring time and distance, and if the mean drag answer be regarded as correct, then the extreme points in the scatter show the order of maximum drag error

due to time and distance errors. The correspondence between the scatter of data and the theoretical error curve is apparent. That the correspondence is not exact is due to the facts that: the maximum error in a given run will generally not be the maximum possible error, depending on how the errors of measurement are distributed; smaller distance errors than the maximum assumed, 0.003 inch, undoubtedly occurred in many cases; and time errors as well as distance errors are involved. Nevertheless, the general validity of the method is well supported by this comparison.

The time error,  $e_t$ , which is equivalent to a given distance error,  $e_x$ , can be found with the aid of the erroneous point shown at time,  $t_i$ , in figure 17. Presuming that such a point has been measured, one does not know if the reason it fails to fall on the exact curve is error in time or in distance or in both. For present purposes, two possibilities will be considered, a pure time error with distance accurate, and a pure distance error with time accurate. The two errors are indicated on the figure and it is apparent that for small errors,

$$e_x/e_t = dx/dt = u_m \quad (21)$$

On the basis of this result, the time errors which are equivalent to a 0.003-inch distance error have been computed and are shown in figure 19 as a function of model velocity. At the lower speeds time errors of the order of 0.1 microsecond are comparable to distance errors of 0.003 inch. As velocity is raised, time measurement must become increasingly accurate to remain comparable to a 0.003-inch distance error.

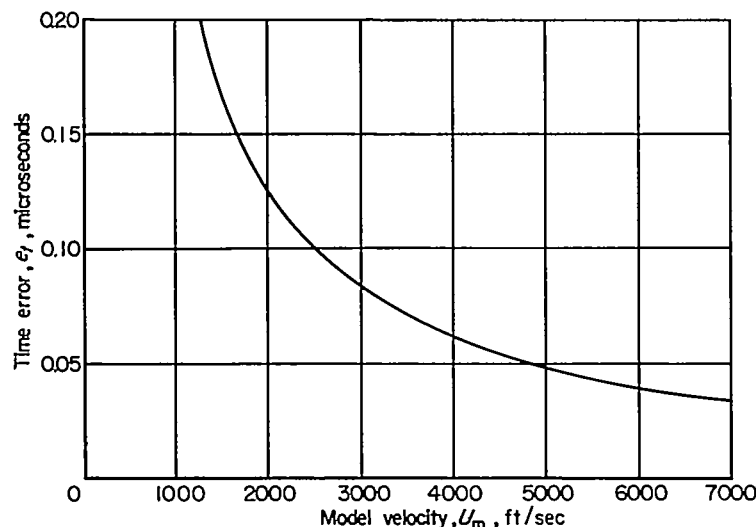


FIGURE 19.—Time errors equivalent to a 0.003-inch distance error.

It was shown in equation (20) and figure 18 that the distance decrement is the essential element in the accuracy problem, so a closer examination of this quantity and the factors that will affect it is indicated. Simply expanding the distance decrement from its definition gives the desired information.

$$d = \frac{1}{2} a t^2 = \frac{1}{2} \frac{D}{m} t^2 = \frac{1}{2} \frac{D}{m} \left( \frac{x_m}{u_m} \right)^2 = C_D \frac{\rho A}{4m} \left( 1 + \frac{u_a}{u_m} \right)^2 x_m^2 \quad (22)$$

Thus the distance decrement depends on the square of the range length and on the first power of the air density and the drag coefficient. The model scale and model density

affect the distance decrement through the ratio  $A:m$ . The larger and denser the model, the smaller the distance decrement becomes. The contribution of the air-stream velocity to the dynamic pressure is in the term,  $[1 + (u_a/u_m)^2]$ , which increases the distance decrement at the lower speeds but becomes less important as  $u_m$  becomes large compared to  $u_a$ . Figure 18 shows that there is a more or less sharply defined critical distance decrement below which drag measurement is inaccurate. The normal approach to drag measurement in the facility is to manipulate the above factors to obtain a satisfactorily large distance decrement.

The time and distance accuracy requirements for drag measurement, then, cannot be stated absolutely as simple numbers but depend on the model distance decrement and on the model velocity. With models of low density and small scale, the requirements are relaxed. In practice, the distance decrements in 15 feet of flight have been held above 1 inch for the most part but have ranged from 0.3 to 15 inches. Drag results with small scatter can be obtained from careful measurements when the distance decrement exceeds 0.5 inch. This is probably the most meaningful way to state the accuracy capabilities of the facility.

Some measurements of the drag of a 60° cone cylinder.—As an example of the drag data obtained, there are shown in figure 20 measurements of the drag of a 60° included angle cone-cylinder at Mach numbers from 1.5 to 8.2. The data below  $M=4.5$  were obtained with still air in the wind-tunnel test section and the remainder were obtained with "air-on." The models were 0.18 inch in diameter, made of brass, encased in lucite sabots to protect their surfaces, and launched from a 0.220 Swift rifle spin-stabilized. As is evident in the figure, the internal consistency of the data is very satisfactory, a little better for the still-air tests than for the tests with air flow. In the latter case, inaccurate determination of the air density at the instant of firing contributed to the scatter. Additional scatter is due to model differences. The average deviation of the experimental points from the curve is 1.2 percent and the worst point is 3.8 percent off the curve. The distance decrements for these models ranged from 1.8 inches to 4.5 inches depending on test conditions. These measurements were reported in reference 5, wherein their relationship to the predicted values of conical wave drag is discussed.

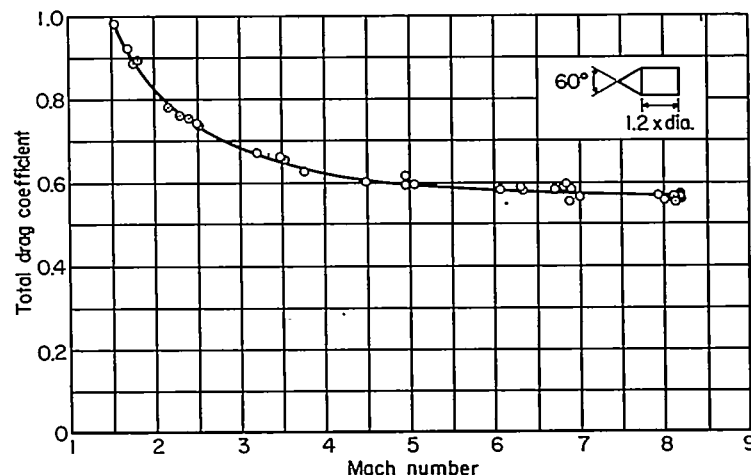


FIGURE 20.—Measured drag coefficients of a cone-cylinder.

## LIFT MEASUREMENT

As was stated at the beginning of this section, lift is computed from measurements of the curvature of the model flight path. To develop the equations needed for this reduction, consider the flight of a model oscillating in pitch about the attitude for zero lift. Assume that the amplitude of oscillation is limited to the range of linear lift and pitching moments so that the oscillation is sinusoidal, and for simplicity, consider the oscillation to be undamped.<sup>7</sup>

$$\alpha = \alpha_M \sin 2\pi ft \quad (23)$$

The lift and acceleration normal to the flight path will then vary sinusoidally.

$$\frac{d^2 y}{dt^2} = \frac{L}{m} = \frac{C_{L\alpha} q A}{m} \alpha_M \sin 2\pi ft \quad (24)$$

Integration gives the time history of lateral position of the model center of gravity,

$$y = -\frac{C_{L\alpha} q A \alpha_M}{m (2\pi f)^2} \sin 2\pi ft \quad (25)$$

From equation (25) and observations of the frequency  $f$ , the amplitude of pitching  $\alpha_M$ , and the lateral position history of the flight, the lift-curve slope can be determined. Initial velocity along  $y$  and phase shifting of the sine wave complicate the equations a little but do not alter the principle.

<sup>7</sup> A very near approximation for the actual flights where the amplitude reduction per cycle is typically less than 5 percent. Of course, the equations can also be written with the damping included.

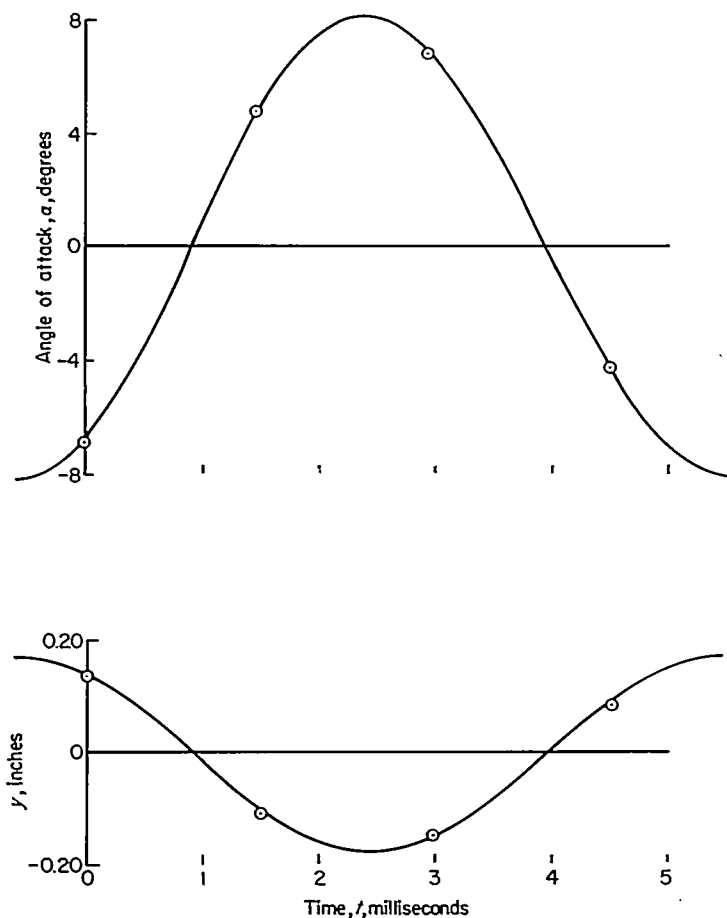


FIGURE 21.—Example of data used to compute  $C_{L\alpha}$ ,  $C_{m\alpha}$ , and  $x_{cp}$ .

The details of application of this procedure are given in reference 1. Some typical data on the pitching oscillation and lateral position history are shown in figure 21. It is possible to determine accurately the lift-curve slope when the departure from straight-line flight is as much as 0.1 inch.

## MEASUREMENT OF STATIC LONGITUDINAL STABILITY

The static longitudinal stability of aerodynamically stable test models is determined from the frequency with which they oscillate in pitch. The frequency is given by the angle-of-attack history to which a damped sine wave is fitted by a least squares procedure as has been done with the data in figure 21. The frequency is related to the moment-curve slope by the equation,

$$M_\alpha = (2\pi f)^2 I_y \quad (26)$$

To locate the center of pressure, it is necessary to know both the moment-curve slope and the lift-curve slope since

$$I_\alpha \alpha (x_{cp} - x_{cg}) = M_\alpha \alpha$$

or

$$\frac{x_{cp} - x_{cg}}{l} = \frac{C_{m\alpha}}{C_{L\alpha}} \quad (27)$$

The margin of stability is the quantity directly obtained. For small static margins, this proves to be an inherently accurate way of locating center of pressure since even large percentage errors in static margin will result in small error in center-of-pressure location.

## MEASUREMENT OF ROLL CHARACTERISTICS

To measure aerodynamic characteristics associated with model rolling motions a photographic record is made of the variations in roll position experienced by a test model in flight. To produce this record, a high-speed motion picture camera in the settling chamber of the wind tunnel is oriented to view the test section along a line approximately parallel to the tunnel axis. Illumination is provided by a searchlight in the wind-tunnel diffuser. With this photographic arrangement, silhouette pictures are obtained of the model in oncoming flight. The camera will record a maximum of 8000 frames per second, so the roll position is recorded on the order of one time per foot of model travel. In figure 22, four frames from such a record show the model rolling perceptibly. The round object above and to the right of the model is the rifled sabot base which trails several feet behind the model. Roll position is measured from these pictures to produce data like that shown in figure 23.

To the measurements of roll position, there is fitted a theoretical curve. The equation of this curve is developed from the differential equation,

$$I_x \frac{d^2 \phi}{dt^2} = l_r \delta + l_p \frac{d\phi}{dt} \quad (28)$$

which describes the resultant rolling acceleration due to control deflection and aerodynamic damping.<sup>8</sup> Integration of equation (28) leads to an expression for roll position as a function of time,

<sup>8</sup> The rolling moment due to rolling velocity,  $l_p$ , is here considered negative when the rolling motion is damped.

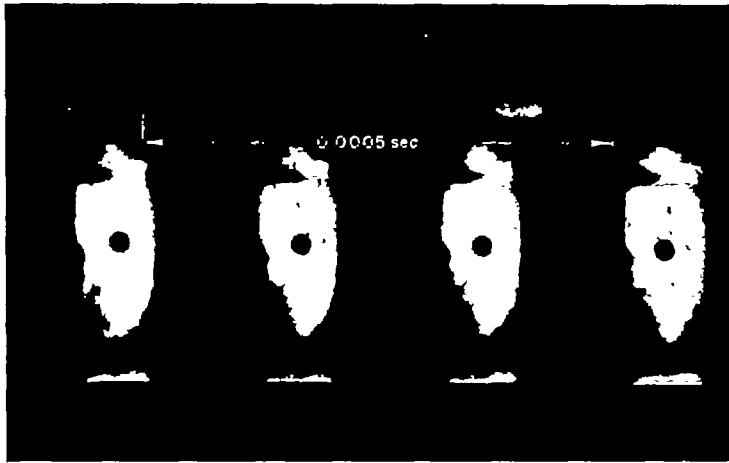


FIGURE 22.—Portion of film record of model roll position.

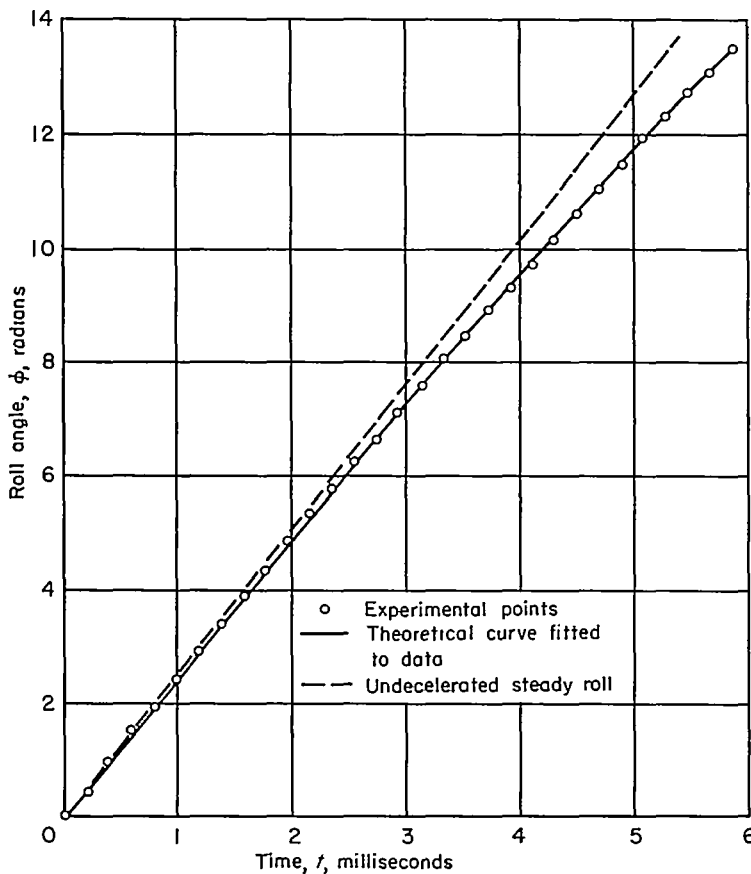


FIGURE 23.—Roll position history of a spinning, fin-stabilized model.

$$\varphi = \varphi_i - \frac{I_x}{l_p} (p_i - p_e) + p_e t + (p_i - p_e) \frac{I_x}{l_p} e^{(l_p/I_x)t} \quad (29)$$

in which only two variables occur,  $\varphi$  and  $t$ . This is emphasized by rewriting equation (29) as

$$\varphi = a_1 + a_2 t + a_3 e^{-kt} \quad (30)$$

Fitting equation (30) to the experimental data by the method described in reference 6 yields values of the constants,  $a_1$ ,  $a_2$ ,  $a_3$ , and  $k$  which, in turn, are directly related to the aerodynamic properties,  $l_\delta$  and  $l_p$ , of the test configuration.

First attempts to apply this procedure to measure the damping in roll of a spinning fin-stabilized body of revolution

were unsatisfactory in that it was found that an unacceptably large range of damping-in-roll coefficients,  $C_{l_p}$ , would permit the theoretical curve to fit the measured roll positions within the accuracy of measurement.<sup>9</sup> Analysis showed the reason for this lack of determination of  $C_{l_p}$ . If equation (28) is written for the particular values of rolling velocity and roll acceleration at the beginning and end stations of the test section, subscripts 1 and 2, respectively,

$$\left. \begin{aligned} I_x \left( \frac{d^2 \varphi}{dt^2} \right)_1 &= l_\delta \delta + l_p \left( \frac{d\varphi}{dt} \right)_1 \\ I_x \left( \frac{d^2 \varphi}{dt^2} \right)_2 &= l_\delta \delta + l_p \left( \frac{d\varphi}{dt} \right)_2 \end{aligned} \right\} \quad (31)$$

then the rolling moment due to accidental wing incidence,  $l_\delta \delta$ , can be eliminated to yield

$$I_x \left[ \left( \frac{d^2 \varphi}{dt^2} \right)_2 - \left( \frac{d^2 \varphi}{dt^2} \right)_1 \right] = l_p \left[ \left( \frac{d\varphi}{dt} \right)_2 - \left( \frac{d\varphi}{dt} \right)_1 \right] \quad (32)$$

In the limit, as the distance between stations 1 and 2 becomes infinitesimal,

$$l_p = I_x \frac{d(d^2 \varphi / dt^2)}{d\varphi} = I_x \frac{d^3 \varphi / dt^3}{d^2 \varphi / dt^2} \quad (33)$$

which shows that the damping-moment coefficient is defined by triple differentiation of the roll-position data. Not only the roll acceleration but changes in roll acceleration must be measured, and the data were not sufficiently precise to yield this information in a working range of 15 feet.

To meet this difficulty, the models were fabricated with great care to reduce the term,  $l_\delta \delta$ , to a negligible value, and thus to make possible the omission of this term from equation (28). The resulting expression for  $l_p$ ,

$$l_p = I_x \frac{d^2 \varphi / dt^2}{d\varphi / dt} \quad (34)$$

shows that only the direct measurement of roll acceleration is then required, and not its rate of change with time. With this simplification, accurate results for  $C_{l_p}$  were immediately obtained.

For measurement of aileron effectiveness,  $l_\delta$ , models with controls deflected are caused to pass through the test section at small rolling velocity so that  $l_p p$  can be neglected compared to  $l_\delta \delta$ . This is achieved by launching the model from a rifled gun spinning in opposition to the deflected control. The model immediately begins to decelerate in roll and the gun position and other factors are regulated to let the model reach zero rolling velocity near the center of the test section. Then

$$l_\delta \delta = I_x \frac{d^2 \varphi}{dt^2} \quad (35)$$

A correction to the measured control effectiveness is subsequently applied for the small remaining average rolling moment due to damping within the test section.

<sup>9</sup> For this test, no control deflection was applied. However, the control-moment term was retained to represent incidence of the wings accidentally produced in model fabrication.

## BOUNDARY-LAYER INVESTIGATIONS

Because the air temperature and body surface temperature conditions of tests in this facility are similar to those occurring in flight, there has been interest in applying the facility to the study of boundary-layer problems. At the time of this writing, investigations of two types have been completed, reported in references 7 and 8, and what is said here will be limited to describing the methods employed to obtain those results. One was a skin-friction investigation and the other was concerned with boundary-layer transition.

The skin friction was determined from drag measurements. A model was selected (shown at the right in fig. 6) having a high ratio of wetted area to frontal area (133:1), so as to develop appreciable skin-friction drag compared to wave drag. However, with the best model that could be made to fly, the skin friction with turbulent flow was still in the range of one-third to two-thirds of the total drag, depending on the Mach number. It was necessary, therefore, to account for the large residual drag, preferably by experiment. To do this, a tare model technique was used. A short tubular model, like the test model in all respects except length, was used for this purpose. The tare model was made to have the same wave drag and the same boundary-layer trip as the test model insofar as the geometry could be duplicated. The skin friction on the extra length of the test model was then obtained by subtracting the measured drag of the tare model from that of the test model. Small corrections were required for minute differences in geometry between the test and tare models. A further correction was made for the small difference in base drag between the test and tare models, using existing data for base drag in two-dimensional flow. Thus, the measurement of skin friction was reduced to the measurement of two drag coefficients. The results of applying this procedure to models with turbulent boundary layer at Mach numbers up to 7.25 are given in reference 7.

Boundary-layer transition has been studied using the shadowgraph pictures. The pictures are quite definite as to where the boundary layer is laminar or turbulent as may be seen in figure 24. Where the boundary layer is laminar, a diffraction pattern appears at the model edge. (This pattern is due to light wave interference and is not a view of the laminar boundary layer in any sense. The same pattern is produced with no flow.) Although not clearly shown in the photographic reproduction of figure 24, the point at which turbulence begins can be found by close examination of the original shadowgraph negative to locate the forwardmost eddies, which may appear at first merely as irregularities in the diffraction pattern. In addition, observation is made of the envelope of Mach wave disturbances which originate at the irregular edge of the turbulent boundary layer and are visible in the stream wherever the boundary layer is turbulent.<sup>10</sup> Comparison of transition points indicated by the eddies and by the Mach waves shows practically exact correlation. Because of the short duration of the shadowgraph sparks, the instantaneous condition of the boundary layer is recorded rather than the time-average value. In general, it is found that the transition point fluctuates on the test models in flight, changing from one shadowgraph station to the next. Study of a complete set of pictures gives a fair sample of the timewise variations that occur. For further information on this test technique and results which have been obtained, see reference 8.

## EFFECT OF AIR-STREAM IMPERFECTIONS ON AERODYNAMIC MEASUREMENTS

The air stream in the Ames supersonic free-flight wind tunnel, as in most supersonic wind tunnels, is imperfect. It is pertinent to examine the effect of the imperfections on the aerodynamic measurements described above. The Mach number, nominally 2, ranges between 1.96 and 2.00 with a mean value of 1.98. Associated with this Mach number variation there are variations in static and dynamic pressure as well as appreciable stream angularity. Fortunately, the test results are not critically dependent on the perfection of the air stream. A model, in flying through the test section, averages the air properties it encounters. Also, it tends to reduce the percentage variation because its motion is equivalent to a component of stream velocity which is free of imperfections. For example, a given lateral component of stream velocity which causes a certain stream angularity relative to a fixed model will cause smaller stream angularity on the moving model because the stream angle will be defined by  $v_a/(u_m + u_a)$ .

The maximum stream angle found in the survey was appreciable,  $0.8^\circ$  for a stationary model. For a test Mach number of 4, the maximum becomes  $0.4^\circ$ , and as the test Mach number is increased to 10, the maximum stream angularity goes to  $0.16^\circ$ . These angles are small compared to the pitching amplitudes normally encountered and occur

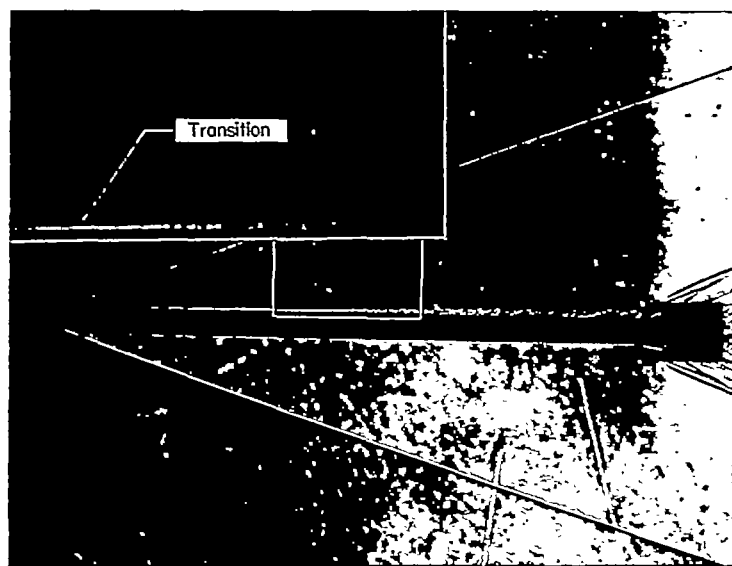


FIGURE 24.—Shadowgraph showing boundary-layer transition on one side of a body of revolution at a Mach number of 3.5 and a length Reynolds number of 12 million.

<sup>10</sup> Distinction must be made between the Mach waves originating from body-fixed disturbances, such as machine marks, and those originating at the irregular edge of the turbulent boundary layer. The former are inclined at about the free-stream Mach angle, whereas the latter are inclined at a Mach angle characteristic of a lower Mach number. This is because the turbulent air is in backward motion along the body and therefore has a lower speed relative to the free stream than does the body.

mainly in the vertical plane so they do not affect pitching motion in a horizontal plane. Furthermore, the frequency of variation of the stream angle is about five times the natural frequency in pitch of the test models so that the pitching response of the models to the impressed variation is weak. It is therefore concluded that no serious error is caused by the stream angularity. The dynamic pressure variation that occurs is a cause of some scatter in the results because the mean dynamic pressure is not precisely equal in the three distance intervals, showing a variation of the order of 0.5 percent. Static pressure gradient along the tunnel axis causes buoyancy forces which are small compared to the drag and can be ignored. Furthermore, they are compensating in effect, being sometimes decelerating and sometimes accelerating in sense. The variations in test Mach number are not significant since appreciable changes in aerodynamic coefficients normally do not occur at high supersonic speed when the test Mach number is changed by the maximum variation that occurs, 0.1. Thus, it appears that the airstream imperfections present do not significantly impair the precision of the results.

#### CONCLUDING REMARKS

The Ames supersonic free-flight wind tunnel is a departure from the conventional approach to the problem of aerodynamic testing at high supersonic Mach numbers. Experience has shown that it is a productive way to study many of the problems of flight in the Mach number range from 2 to 10. Although it appeared at first that the short test section would limit the capabilities of the wind tunnel, careful attention to model design, particularly in regard to model mass and moment of inertia, and development of suitably accurate instruments for measuring position and attitude as a function of time have made it possible to measure accurately the drag, initial lift-curve slope, and center of pressure of a wide variety of configurations. Some fundamental advantages of the facility are that the stagnation temperatures it develops are nearly as great as in free flight through the

atmosphere and the Reynolds numbers are relatively high due to the fact that the tests are conducted in air of near atmospheric density at all Mach numbers. These features make the facility a technically feasible and valuable tool for studying boundary-layer problems under the heat-transfer conditions of flight.

The extension of this facility to higher Mach numbers appears feasible. By use of a Mach number 3 air-stream and model velocities only slightly in excess of those currently attained, test Mach numbers up to 15 can be realized.

AMES AERONAUTICAL LABORATORY

NATIONAL ADVISORY COMMITTEE FOR AERONAUTICS

MOFFETT FIELD, CALIF., May 11, 1955

#### REFERENCES

1. Seiff, Alvin, James, Carlton S., Canning, Thomas N., and Boissevain, Alfred G.: The Ames Supersonic Free-Flight Wind Tunnel. NACA RM A52A24, 1952.
2. Briggs, Robert O., Kerwin, William J., and Schmidt, Stanley F.: Instrumentation of the Ames Supersonic Free-Flight Wind Tunnel. NACA RM A52A18, 1952.
3. Charters, A. C.: Some Ballistic Contributions to Aerodynamics. Jour. Aero. Sci., vol. 14, no. 3, 1947, pp. 155-166.
4. Kovasznay, Leslie S. G.: High Power Short Duration Spark Discharge. The Review of Scientific Instruments, vol. 20, no. 9, Sept. 1949, pp. 696-697.
5. Seiff, Alvin, and Sommer, Simon C.: Experimental Investigation of the Drag of 30°, 60°, and 90° Cone Cylinders at Mach Numbers Between 1.5 and 8.2. NACA RM A52A14b, 1952.
6. Bolz, Ray E., and Nicolaides, John D.: A Method of Determining Some Aerodynamic Coefficients from Supersonic Free Flight Tests of a Rolling Missile. BRL Rep. 711, Aberdeen Proving Ground, Aberdeen, Md., Dec. 1949. (Also issued as I. A. S. Preprint 252, 1950).
7. Sommer, Simon C., and Short, Barbara J.: Free-Flight Measurements of Turbulent-Boundary-Layer Skin Friction in the Presence of Severe Aerodynamic Heating at Mach Numbers From 2.8 to 7.0. NACA TN 3391, 1955.
8. Jedlicka, James R., Wilkins, Max E., and Seiff, Alvin: Experimental Determination of Boundary-Layer Transition on a Body of Revolution at  $M=3.5$ . NACA TN 3342, 1954.

